



Cite this: *RSC Adv.*, 2019, 9, 33572

# Study on MnO<sub>2</sub>/MXene–Ti<sub>3</sub>C<sub>2</sub> composite materials as cathode materials for magnesium batteries

Yuan Li,  Donghui Xu, Dehang Zhang, Yuanchi Wei, Ruinan Zhang and Yuxiang Guo\*

In this paper, MnO<sub>2</sub>/MXene–Ti<sub>3</sub>C<sub>2</sub> composites with different molar ratios were successfully prepared by a one-step hydro-thermal method, and the optimum proportion was confirmed by XRD and SEM comparative analysis. The optimum proportion of MnO<sub>2</sub>/MXene–Ti<sub>3</sub>C<sub>2</sub> composites and MnO<sub>2</sub> was used as a cathode material for magnesium batteries to carry out the electrochemical performance test. The results showed that the charge–discharge capacity of the MnO<sub>2</sub>/MXene–Ti<sub>3</sub>C<sub>2</sub> composite was up to 105 mA h g<sup>−1</sup>, much higher than that of MnO<sub>2</sub> (64 mA h g<sup>−1</sup>), and meanwhile it had good rate performance. At the same time, this also opened up the application of MXene–Ti<sub>3</sub>C<sub>2</sub>, a new two-dimensional material, in the field of battery electrode materials.

Received 21st September 2019  
Accepted 11th October 2019

DOI: 10.1039/c9ra07652b

rsc.li/rsc-advances

## 1. Introduction

With the rapid development of social economy, increasing consumption of fossil energy and escalating environmental pollution, it is extremely urgent to find clean, environmentally friendly, efficient and sustainable energy sources.<sup>1–3</sup> Therefore, some new environmentally friendly secondary batteries with high-capacity have been favored by domestic and overseas researchers. Among them, lithium-ion batteries are widely used because of their high energy density and mature technology, but they have the problems of high cost and poor safety.<sup>4,5</sup> Magnesium and lithium are located in a diagonal position in the periodic table, and have similar ionic radii and chemical properties. Compared with lithium metal (180.5 °C), the melting point of magnesium (648.8 °C) is much higher, and its activity is poorer. So, it is easy to process and also safer. Moreover, magnesium ions can carry two charges. Although the mass specific capacity (2205 mA h g<sup>−1</sup>) is not as high as lithium metal (3862 mA h g<sup>−1</sup>), it is still considerable.<sup>6–9</sup> At the same time, China is rich in magnesium resources, ranking first in the world, and the price is low and it's easy to obtain.<sup>10–12</sup> So, magnesium ion batteries have attracted much attention from researchers around the world.

Based on advanced theoretical algorithms, modeling, simulation, and computer technology, the reasonable design of materials, batteries, devices and batteries in the field of lithium ion batteries is gradually being realized.<sup>13,14</sup> Some researchers have also used the first principle to do research about the stability on electrode materials for magnesium batteries.<sup>15</sup> The calculation and experiment of large shared database connection

can greatly help to narrow some of the current experimental and technical gaps, as well as predict the path-independent characteristics, and help to fundamentally understand the path-independent performance in multiple space-time scales.

Magnesium ion battery is mainly composed of three parts: compound cathode which can reversibly imbed–detach magnesium ion, metal magnesium and its alloy's negative electrode, and electrolyte.<sup>16–18</sup> When discharging, the metal magnesium of the negative electrode dissolves out and forms the magnesium ion. It reaches the positive electrode through a series of processes such as dissolution, adsorption and transfer of electrolyte, and then it is embedded in the cathode materials. When charging, the magnesium ions embedded in the cathode material are detached and reach the negative electrode under the action of external electric field, and then they are deposited again to form the metal magnesium.<sup>19–22</sup>

At present, the studies on magnesium ion batteries at home and abroad mainly focus on cathode materials and electrolytes, which are all still in the preliminary stage. Cathode material is the key factor which restricts the development of magnesium ion battery, and some domestic and overseas scholars are trying to find and develop new cathode materials.<sup>23–25</sup> MnO<sub>2</sub> is a kind of electrode material with high theoretical specific capacity, low cost and easy availability, which has been widely used as battery electrode material, but its poor conductivity and stability limit the application of MnO<sub>2</sub> as electrode material.<sup>26–28</sup> Therefore, many researchers have improved the electrochemical performance of MnO<sub>2</sub> by improving MnO<sub>2</sub>'s nanostructure or combining MnO<sub>2</sub> with some conductive materials.<sup>29–32</sup>

MXene is a new type of transition metal carbide, carbonitride and nitride (which are collectively called MXene) with two-dimensional graphene-like structure. The general formula of MXene is M<sub>n+1</sub>X<sub>n</sub>T<sub>x</sub> (*n* = 1, 2, 3), of which is an early transition

Department of Materials & Metallurgy, University of Science and Technology Liaoning, Anshan, 114051, China. E-mail: gyxwsd@126.com



metal, X is carbon or nitrogen, and  $T_x$  represents  $O^{2-}$ ,  $OH^-$ ,  $F^-$  and other surfaces functional group, MXene has been widely used in various fields.<sup>33–35</sup> MXene is mainly obtained by selectively etching a fixed atomic layer in the MAX phase of the precursor. MAX phase is the general term of a class of ternary layered compounds, which have a uniform chemical formula  $M_{n+1}AX_n$  (A is III, IV main group elements). Common chemical etchants are hydrofluoric acid or a mixture of hydrochloric acid and lithium fluoride.<sup>36–38</sup> MXene is a new type of two-dimensional layered material, which has the following advantages as electrode material: (1) good electrical conductivity, which is conducive to the electron transmission; (2) large specific surface area, which can provide more storage sites; (3) layered structure, which is conducive to the rapid diffusion of electrolyte ions between layers, providing excellent rate performance; (4) high density of magnesium metal, which makes the volume specific capacity high; (5) adjustable surface chemical structure, which means different MXene can provide different working potential windows.<sup>39–43</sup> So far  $Ti_3C_2T_x$  is the most studied MXene. It has been successfully used as electrode material for supercapacitors, sodium-ion batteries and lithium-ion batteries.<sup>44–46</sup> Among them,  $Ti_3C_2T_x$  as electrode material for lithium ion battery is the most widely studied. Some researchers have also prepared some  $Ti_3C_2T_x$  matrix composites for lithium batteries and shows excellent capacity and rate performance.<sup>47,48</sup> Moreover, MXene has excellent optical, mechanical and thermal stability properties, and has a wide range of applications in the fields of electromagnetic shielding, water treatment, gas, biosensor and photo electrochemistry catalyze.<sup>49,50</sup>

According to the advantages of MXene—a new type of material, we deposited  $MnO_2$  nanoparticles on the surface of MXene- $Ti_3C_2$  material with high specific surface areas and high electrical conductivity by hydro-thermal method in this article, and its electrochemical performance was tested as the cathode for magnesium batteries.

## 2. Experimental section

### 2.1 Preparation of manganese dioxide

Firstly, 145.29 mg of potassium permanganate was weighed and placed into the beaker; added 50 mL distilled water, stirred it for 30 minutes to fully dissolve. Then the solution was transferred to the hydro-thermal reactor and reacted at 150 °C for 20 h. After the reaction is over, take out the hydro-thermal reactor and cool it to room temperature. After cooling, the samples were centrifugally washed with alcohol and water alternately for 6–8 times. After that the samples were transferred to the beaker and dried in vacuum for 24 h at 60 °C, then it became the manganese dioxide.

### 2.2 Preparation of MXene- $Ti_3C_2$

Firstly, 2 g of  $Ti_3AlC_2$  2 g and lithium fluoride were respectively accurately weighed; 40 mL of hydrochloric acid (HCl, 9 M) was weighed using a measuring cylinder and was poured slowly into a beaker. Added 2 g of lithium fluoride and stirred it for 60 minutes; added 2 g of  $Ti_3AlC_2$  slowly into the mixed solution; then magnetically stirred it at room temperature (25 °C) for 24 h at a speed of

200 rpm; repeated washing it ultrasonically centrifugally with deoxidized water until the pH value reaches 6; dried the sediment in vacuum at 120 °C for standby use, and this is the MXene- $Ti_3C_2$ .

### 2.3 Preparation of $MnO_2$ /MXene- $Ti_3C_2$ composites

Firstly, 40 mg of  $Ti_3C_2T_x$  was weighed and placed in the beaker; added 50 mL distilled water, ultrasonically stirred it for 30 minutes; 145.29 mg of potassium permanganate with the mole ratio of 1 : 1 was weighed and fully mixed for 30 min. Then poured the stirred solution into the hydrothermal reactor, and set the temperature at 150 °C and the time at 20 h. After the reaction is over, the reaction still was taken out and cooled to room temperature. After cooling, the resulting solution was centrifuged to get the underlayer sediment; the sediment was washed with absolute ethyl alcohol and distilled water alternately for 6–8 times. The washed sample was put into the beaker and dried in a vacuum drying box at 60 °C for 24 h to obtain  $MnO_2$ /MXene- $Ti_3C_2$  composites.

When preparing  $MnO_2$ /MXene- $Ti_3C_2$  composites with molar ratios of 1 : 2, 1 : 1 and 2 : 1, the mass of  $KMnO_4$  was maintained the same, and different mass of MXene- $Ti_3C_2$  mixtures were weighed respectively for reaction, which was consistent with the above-mentioned process.

## 3. Results and discussion

### 3.1 XRD and SEM analysis

Fig. 1 shows the XRD spectrums of  $MnO_2$  and  $MnO_2$ /MXene- $Ti_3C_2$  nanocomposites with different molar ratios. It can be seen from the figure that there are obvious diffraction peaks in  $MnO_2$  sample at  $2\theta$  of 12.77°, 24.78°, 36.55° and 66°, corresponding to (003), (006), (012) and (110) crystal planes of the  $\delta$ - $MnO_2$  standard card (JCPDS 01-086-0666) respectively.<sup>51–53</sup> No other phase substances were detected in the spectrums, indicating that the layered  $\delta$ - $MnO_2$  is successfully prepared. From the XRD diffraction spectrums of MXene- $Ti_3C_2$ , by comparing and analyzing the standard cards of precursor  $Ti_3AlC_2$  in other papers, it can be seen that when  $2\theta$  was 9.0°, 16.21°, 18.32°, 34.26°, 52.88° and 60.81°, it was corresponding to the crystal

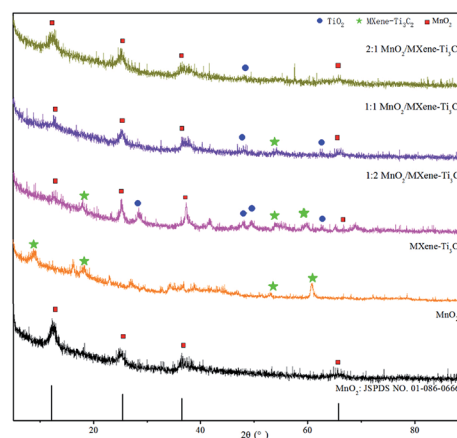


Fig. 1 X-ray diffraction analysis results.



planes of (002), (004), (006), (0010), (0012) and (110) respectively, these are the characteristic diffraction peaks of MXene- $\text{Ti}_3\text{C}_2$ , which are consistent with other reports.<sup>54,55</sup> In the XRD spectrums of  $\text{MnO}_2/\text{MXene-Ti}_3\text{C}_2$  composites with molar ratio of 1 : 2, the characteristic diffraction peaks of  $\text{MnO}_2$  and MXene- $\text{Ti}_3\text{C}_2$  appeared, which indicated that  $\text{MnO}_2$  was successfully loaded on the MXene- $\text{Ti}_3\text{C}_2$ ,  $\text{MnO}_2/\text{MXene-Ti}_3\text{C}_2$  composites are successfully prepared. But there is a main peak at  $26.5^\circ$  which illustrates that MXene- $\text{Ti}_3\text{C}_2$  is easy to be oxidized to form  $\text{TiO}_2$  in the hydro-thermal reaction. Moreover, the characteristic diffraction peaks of MXene- $\text{Ti}_3\text{C}_2$  were obviously weakened after adding  $\text{MnO}_2$ . In the XRD spectrums of  $\text{MnO}_2/\text{MXene-Ti}_3\text{C}_2$  composites with molar ratio of 1 : 1 and 2 : 1, the characteristic diffraction peaks of  $\text{MnO}_2$  appeared, but the characteristic diffraction peaks of MXene- $\text{Ti}_3\text{C}_2$  gradually weakened and disappeared, showing that  $\text{MnO}_2$  nanoparticles can inhibit the recrystallization of two-dimensional MXene- $\text{Ti}_3\text{C}_2$  lamellae in  $\text{MnO}_2/\text{MXene-Ti}_3\text{C}_2$  composites, and the larger the proportion, the more obvious the effect.

Fig. 2 is the scanning electron microscope images of the samples at different multiples. It can be seen from the Fig. 2a that MXene- $\text{Ti}_3\text{C}_2$  has a layered structure similar to the organ, and the nanosheet of MXene- $\text{Ti}_3\text{C}_2$  are tightly bonded together, so the large specific surface area of MXene- $\text{Ti}_3\text{C}_2$  can not be fully utilized. Fig. 2b is a typical SEM image of layered  $\text{MnO}_2$ . It can be seen that  $\text{MnO}_2$  is formed by overlapping and agglomeration of nanosheet layers into three-dimensional flower bract shape. The interspace of nanosheet layers is large which forms abundant pore structures.<sup>56–59</sup> Fig. 2c is a SEM image of  $\text{MnO}_2/\text{MXene-Ti}_3\text{C}_2$  nanocomposites with molar ratio of 1 : 2, from which we can see that  $\text{MnO}_2$  is evenly distributed between the nanosheet layers and the interspace of MXene- $\text{Ti}_3\text{C}_2$ . At the same time, there are some irregular nanoparticles on the surface and between layers of MXene- $\text{Ti}_3\text{C}_2$ , which consistent with the XRD analysis above. So MXene- $\text{Ti}_3\text{C}_2$  is easy to be oxidized to form  $\text{TiO}_2$  in the hydro-thermal reaction. Because MXene- $\text{Ti}_3\text{C}_2$  is obtained by removing A by etching MAX through HF, some surface functional groups will be produced

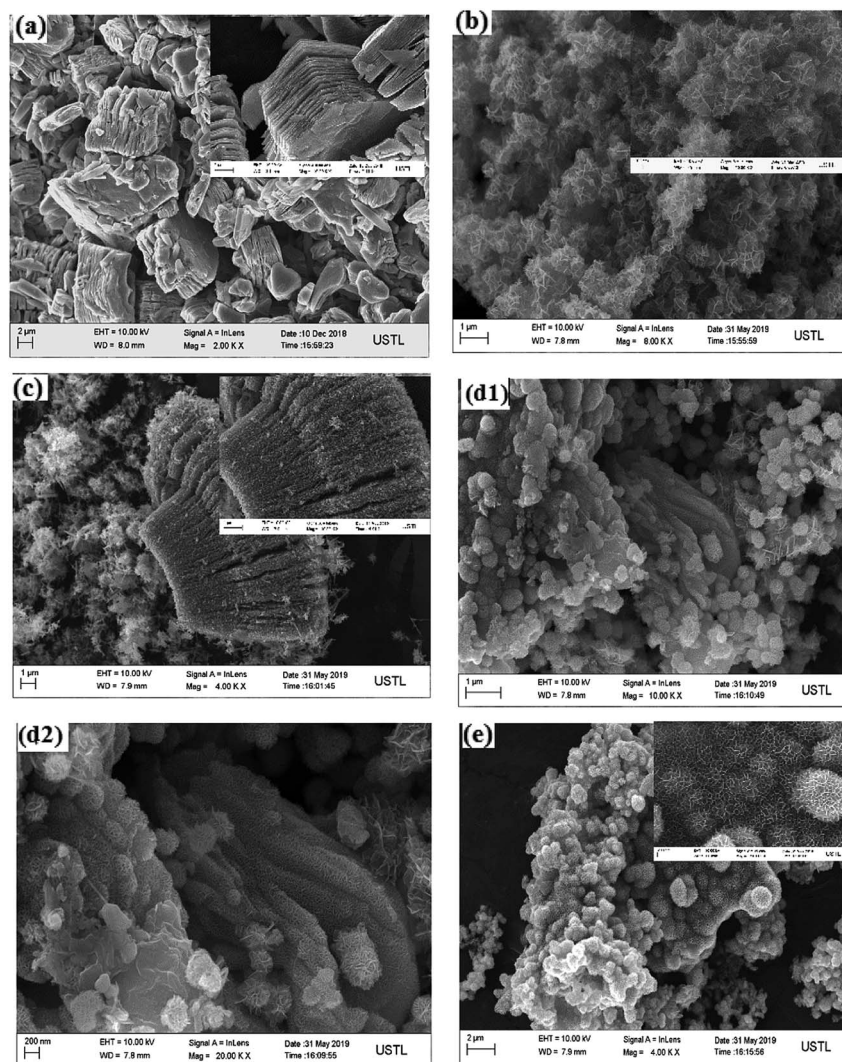


Fig. 2 (a) SEM image of MXene- $\text{Ti}_3\text{C}_2$  material. (b) SEM image of  $\text{MnO}_2$  material. (c)–(e) is the  $\text{MnO}_2/\text{MXene-Ti}_3\text{C}_2$  nanocomposites with molar ratio 1 : 2, 1 : 1 and 2 : 1 in sequence.





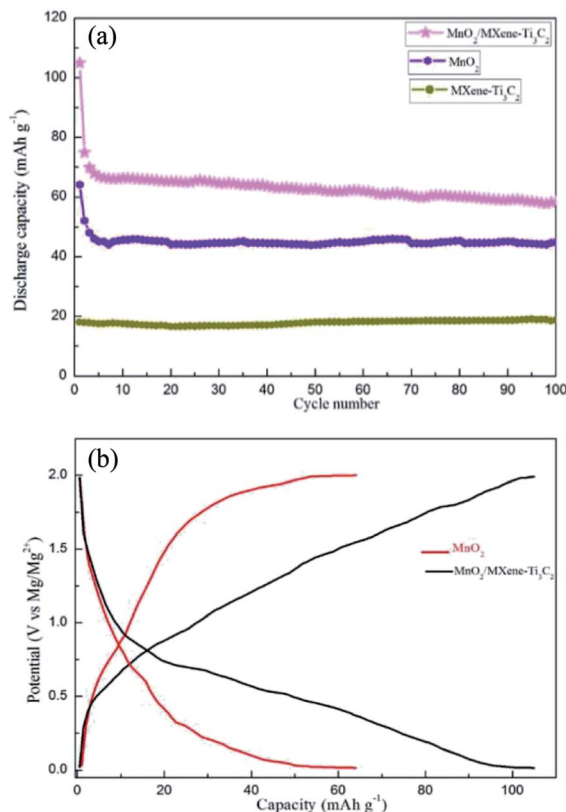


Fig. 3 (a) Cycle performance of MXene-Ti<sub>3</sub>C<sub>2</sub>, MnO<sub>2</sub> and MnO<sub>2</sub>/MXene-Ti<sub>3</sub>C<sub>2</sub> composites with the molar ratio of 1 : 2. (b) Capacity-potential diagram of MnO<sub>2</sub> and MnO<sub>2</sub>/MXene-Ti<sub>3</sub>C<sub>2</sub>.

during etching and some defects may occur at the edge of MXene-Ti<sub>3</sub>C<sub>2</sub> lamellae. These defects and active sites provided by surface functional groups create conditions for the uniform distribution of MnO<sub>2</sub>. Fig. 2d1 and d2 is a SEM image of MnO<sub>2</sub>/MXene-Ti<sub>3</sub>C<sub>2</sub> nanocomposites with molar ratio of 1 : 1 at different multiples. From Fig. 2d1, we can see that MnO<sub>2</sub> nanospheres and some agglomerated TiO<sub>2</sub> particles are closely accumulated on MXene-Ti<sub>3</sub>C<sub>2</sub> lamellae, wrapping MXene-Ti<sub>3</sub>C<sub>2</sub> sheet lamellae, and the structure of MXene-Ti<sub>3</sub>C<sub>2</sub> can hardly be seen. As can be seen in Fig. 2d2, MXene-Ti<sub>3</sub>C<sub>2</sub> lamellae surfaces are densely packed with spherical MnO<sub>2</sub>, which seriously hinders the effect of MXene-Ti<sub>3</sub>C<sub>2</sub>. Fig. 2e is a SEM image of

MnO<sub>2</sub>/MXene-Ti<sub>3</sub>C<sub>2</sub> nanocomposites with molar ratio of 2 : 1. In the picture we cannot see any MXene-Ti<sub>3</sub>C<sub>2</sub> substance. There were all nano MnO<sub>2</sub> with flower sphere shape. The flower spheres are tightly packed together, forming a honeycomb three-dimensional structure. In conclusion, when the molar ratio of MnO<sub>2</sub> to MXene-Ti<sub>3</sub>C<sub>2</sub> is 1 : 2, they are evenly combined. With the increase of molar ratio, the MXene-Ti<sub>3</sub>C<sub>2</sub> substance decreases and disappears gradually. The increase of MnO<sub>2</sub> inhibits the recrystallization of MXene-Ti<sub>3</sub>C<sub>2</sub>.

### 3.2 Electrochemical performance analysis

As shown in Fig. 3a, the capacity of MXene-Ti<sub>3</sub>C<sub>2</sub> as cathode material for magnesium batteries is 18 mA h g<sup>-1</sup> at 50 mA g<sup>-1</sup> current density, which is low. This is consistent with other literature reports. The first discharge capacity of MnO<sub>2</sub> at 50 mA g<sup>-1</sup> current density is only 64 mA h g<sup>-1</sup>, which is reduced to 45 mA h g<sup>-1</sup> after 100 cycles. When 1 : 2 MnO<sub>2</sub>/MXene-Ti<sub>3</sub>C<sub>2</sub> composite is used as cathode material of magnesium battery, the first discharge capacity is 105 mA h g<sup>-1</sup>, which is much higher than that of other manganese dioxide matrix composites. And after 100 cycles, the discharge capacity is 58 mA h g<sup>-1</sup>, the cycling performance is better than that of Mn<sub>2</sub>. After adding the MXene-Ti<sub>3</sub>C<sub>2</sub>, the capacity of the composite material is greatly improved, which is due to the addition of MXene-Ti<sub>3</sub>C<sub>2</sub> which has large specific surface area and high electrical conductivity, providing more storage sites for the entry and exit of magnesium ions during the working of magnesium batteries, and shortening the transport path of magnesium ions. Fig. 3b shows the voltage-capacity curves of the two samples in the range of 0.01–2.0 V, and the average voltage is 1.0 V. The discharge curves are similar to those of capacitive storage electrode materials. As shown in Fig. 3b, we can see the MoO<sub>2</sub>/MXene-Ti<sub>3</sub>C<sub>2</sub> displays that most capacity does not come from characteristic behaviors of MoO<sub>2</sub> from the slope between 0.2–1.0 V for the composite. Because we added some carbon black as conductive agent in the process of assembling the electrode sheet, it is also beneficial to improve the capacity.

Fig. 4 shows the CV curves of the MnO<sub>2</sub> and MnO<sub>2</sub>/MXene-Ti<sub>3</sub>C<sub>2</sub> composites in the voltage range of 0.01–2.0 V. Compared with MnO<sub>2</sub>, MnO<sub>2</sub>/MXene-Ti<sub>3</sub>C<sub>2</sub> composite material has obvious anode and cathode current response, large CV area and obvious capacity. The CV curve shows a sharp peak when it's

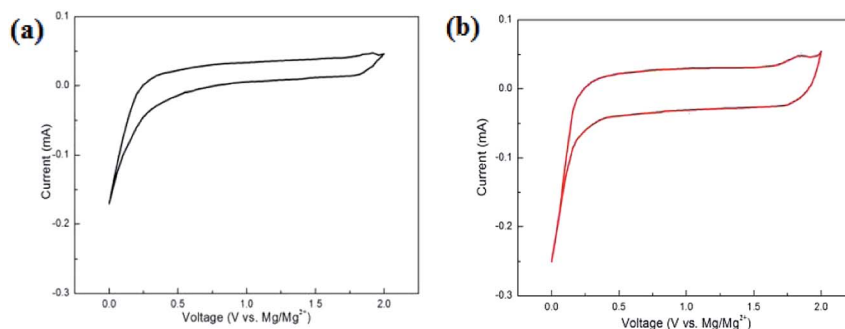


Fig. 4 CV figure of (a) MnO<sub>2</sub> and (b) MnO<sub>2</sub>/MXene-Ti<sub>3</sub>C<sub>2</sub>.



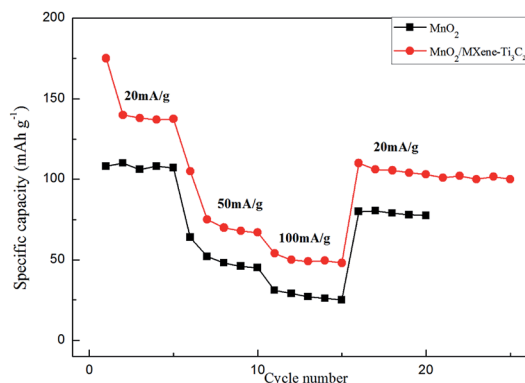


Fig. 5 Rate performance of  $\text{MnO}_2$  and  $\text{MnO}_2/\text{MXene-Ti}_3\text{C}_2$ .

lower than 0.2 V, which may be due to  $\text{Mg}^{2+}$  embedded at the active site of the electrode with high activation energy. This is consistent with the relatively flat discharge curve in the low voltage region of 0.01–0.2 V shown in Fig. 3b. However, after the battery is stabilized, the curve of charge and discharge voltage between 0.01–2.0 V no longer shows a clear charge and discharge platform, which is similar to the charge and discharge curve of capacitor storage, indicating that the main energy storage mechanism of  $\text{MnO}_2/\text{MXene-Ti}_3\text{C}_2$  sample is embedded pseudocapacitance, and the coulombic efficiency of the electrode material is close to 100%.  $\text{MnO}_2/\text{MXene-Ti}_3\text{C}_2$  sample has good cycle performance.

$\text{MnO}_2/\text{MXene-Ti}_3\text{C}_2$  composite electrodes also show excellent rate performance. As shown in Fig. 5, at high current densities of  $100 \text{ mA g}^{-1}$ , the capacities are  $54 \text{ mA h g}^{-1}$ , which are much higher than those of  $\text{MnO}_2$ . In the first ten circles, there is some attenuation of capacity, which is due to the strong electrostatic interaction between  $\text{Mg}^{2+}$  and electrode materials, and  $\text{Mg}^{2+}$  is easy to be captured by some active sites. At a high current density of  $100 \text{ mA g}^{-1}$ , the battery still has a stable capacity of  $54 \text{ mA h g}^{-1}$  and still has a high capacity at a wide range of current densities, indicating that  $\text{MnO}_2/\text{MXene-Ti}_3\text{C}_2$  is a very nice high rate cathode material for magnesium batteries.

## 4. Conclusion

$\text{MnO}_2$  and  $\text{MnO}_2/\text{MXene-Ti}_3\text{C}_2$  composites with different molar ratios are successfully prepared by one-step hydrothermal method in this paper. When the molar ratio was 1 : 2,  $\text{MnO}_2$  evenly adhered on and between  $\text{MXene-Ti}_3\text{C}_2$  lamella, and the composite effect was the best, which was conducive to the imbedding and separation of magnesium ions. When 1 : 2  $\text{MnO}_2/\text{MXene-Ti}_3\text{C}_2$  composite is used as cathode material of magnesium battery, the main energy storage mechanism is embedded pseudo capacitance. The first discharge capacity at  $50 \text{ mA g}^{-1}$  current density is  $105 \text{ mA h g}^{-1}$ , which is much higher than that of  $\text{MnO}_2$ . Even at a high current density of  $500 \text{ mA g}^{-1}$ , the  $\text{MnO}_2/\text{MXene-Ti}_3\text{C}_2$  composite battery still has a stable capacity of  $21 \text{ mA h g}^{-1}$  and good rate performance. At the same time,  $\text{MXene-Ti}_3\text{C}_2$  substrate material with high

conductivity is very valuable for the study of new electrode materials.

## Funding

This work was supported by the Magnesium Industry Collaborative Innovation Center of University of Science and Technology Liaoning (USTLXT201801), Liaoning Natural fund project (2019-ZD-0027) and National Science and Technology Support Plan (2014BAB02B01).

## Conflicts of interest

There are no conflicts to declare.

## Acknowledgements

We would like to thank the reviewers for their kind and valuable comments. The authors thankfully acknowledge the School of High Temperature Materials and Magnesium Resources Engineering, University of Science and Technology Liaoning for their support.

## Notes and references

- 1 Z. Yang, J. Zhang and M. Kintner, *Chem. Rev.*, 2011, **111**, 3577–3613.
- 2 B. Dunn, H. Kamath and J.-M. Tarascon, *Science*, 2011, **334**, 928–935.
- 3 H. D. Yoo, I. Shterenberg and Y. Gofer, *Environ. Eng. Sci.*, 2013, **6**, 2265–2279.
- 4 B. Peng, J. Liang, Z. Tao and J. Chen, *J. Mater. Chem. A*, 2009, **19**, 2877.
- 5 Q. F. Li and N. J. Bjerrum, *J. Power Sources*, 2002, **110**, 1–10.
- 6 X. Zhou, R. K. Guduru and P. Mohanty, *J. Mater. Chem. A*, 2013, **1**, 2757–2780.
- 7 R. Chevrel, M. Seigent and J. Prigent, *J. Solid State Chem.*, 1971, **3**, 515–519.
- 8 P. G. Bruce, F. Krok, J. L. Nowinski and V. C. Gibson, *J. Mater. Chem. A*, 1991, **1**, 705–706.
- 9 P. G. Bruce, F. Krok, J. L. Nowinski and V. C. Gibson, *Solid State Ionics*, 1992, **1**, 351–355.
- 10 C. Potzies and K. U. Kainer, *Adv. Energy Mater.*, 2004, **6**, 281–289.
- 11 A. A. Luo, *J. Magnesium Alloys*, 2013, **1**, 2–22.
- 12 F. Czerwinski, *Corros. Sci.*, 2014, **86**, 1–16.
- 13 S. Q. Shi, J. Gao, Y. Liu, Y. Zhao, W. Qu, W. W. Ju, C. Y. Ouyang and R. J. Xiao, *Chin. Phys. B*, 2016, **25**, 018212.
- 14 Y. H. Cui, Y. Zhao, H. Chen, K. Y. Wei, S. Ni, Y. X. Cui and S. Q. Shi, *Appl. Surf. Sci.*, 2018, **433**, 1083–1093.
- 15 M. M. Huie, D. C. Bock, E. S. Takeuchi, A. C. Marschiloka and K. J. Takeuchi, *Coord. Chem. Rev.*, 2015, **287**, 15–27.
- 16 Y. Liu, L. Jiao, Q. Wu, J. Du, Y. Zhao, Y. Si, Y. Wang and H. Yuan, *J. Mater. Chem. A*, 2013, **1**, 5822–5826.
- 17 Y. L. Liang, R. Feng, S. Q. Yang, H. Ma, J. Liang and J. Chem, *Adv. Mater.*, 2010, **23**, 640–643.



- 18 Q. Y. Si, X. L. Dai, Z. Tianran, T. L. Zhang and J. Chen, *J. Phys. Chem. C*, 2012, **116**, 1307–1312.
- 19 M. Levi, E. Lancry, E. Levi, H. Gizbar, H. Gofer and D. Aurbach, *Solid State Ionics*, 2005, **176**, 1695–1699.
- 20 E. Levi, Y. Gofer, Y. Vestfreed, E. Lancry and D. Aurbach, *Chem. Mater.*, 2002, **14**, 2767–2773.
- 21 A. Mitelman, M. Levi, E. Lancry, E. Levi and D. Aurbach, *Chem. Commun.*, 2007, **41**, 4212–4214.
- 22 P. Lightfoot, F. Erok and J. L. Nowinski, *J. Mater. Chem. A*, 1992, **2**, 139–150.
- 23 K. Naoaki, K. Shinichi, S. Hiroiki and K. Nobuko, *J. Power Sources*, 2001, **97–98**, 515–517.
- 24 I. Tetsu, A. Takero, Y. Shunsuke and D. Takayuki, *J. Mater. Chem. A*, 2011, **21**, 11764–11772.
- 25 Z. Z. Feng, J. Yang, Y. N. Nuli, J. L. Wang, X. J. Wang and Z. X. Wang, *Electrochem. Commun.*, 2008, **10**, 1291–1294.
- 26 T. Shinomiya, V. Gupta and N. Miura, *Electrochim. Acta*, 2006, **51**, 4412–4419.
- 27 X. Wang, A. Yuan and Y. Wang, *J. Power Sources*, 2007, **172**, 1007–1011.
- 28 A. Yuan and Q. L. Zhang, *Electrochem. Commun.*, 2006, **8**, 1173–1178.
- 29 Z. Lin, D. Sun, Q. Huan, J. Yang, M. W. Barsoum and X. Yan, *J. Mater. Chem. A*, 2015, **3**, 14096–14100.
- 30 L. Li, Z. A. Hu and N. An, *J. Phys. Chem. C*, 2014, **118**, 22865–22872.
- 31 Z. Lin, D. Sun, Q. Huang, J. Yang, M. W. Barsoum and X. Yan, *J. Mater. Chem. A*, 2015, **3**, 14201–14210.
- 32 S. Deng, X. Xiao and G. Chen, *Electrochim. Acta*, 2016, **196**, 316–327.
- 33 P. Xu, K. Ye and D. Cao, *J. Power Sources*, 2014, **268**, 204–211.
- 34 M. Naguib, V. N. Mochalin and M. W. Barsoum, *Adv. Mater.*, 2013, **26**, 992–1005.
- 35 M. Naguib, M. Kurtoglu and V. Presser, *Adv. Mater.*, 2011, **23**, 4248.
- 36 Q. Peng, J. Guo and Q. Zhang, *J. Am. Chem. Soc.*, 2014, **136**, 4113–4116.
- 37 M. R. Lukatskaya, O. Mashtalir and C. E. Ren, *Science*, 2013, **341**, 1502.
- 38 J. Halim, K. M. Cook, M. Naguib, P. Eklund, Y. Gogotsi and J. Rosen, *Appl. Surf. Sci.*, 2016, **362**, 406–417.
- 39 Y. Ying, Y. Liu, X. Wang, Y. Mao, W. Cao, P. Hu and X. Peng, *ACS Appl. Mater. Interfaces*, 2015, **7**, 1795–1803.
- 40 X. Wang, X. Shen, Y. Gao, Z. Wang, R. Yu and L. Chen, *J. Am. Chem. Soc.*, 2015, **137**, 2715–2721.
- 41 J. Li, X. Yuan, C. Lin, Y. Yang, L. Xu, X. Du, J. Xie, J. Lin and J. Sun, *Adv. Energy Mater.*, 2017, **7**, 1602725.
- 42 M. Naguib, J. Come, B. Dyatkin, V. Presser, P.-L. Taberna, P. Simon, M. W. Barsoum and Y. Gogotsi, *Electrochem. Commun.*, 2012, **16**, 61–64.
- 43 Z. Lin, D. Sun, Q. Huang, J. Yang, M. W. Barsoum and X. Yan, *J. Mater. Chem. A*, 2015, **3**, 14096–14100.
- 44 X. Wang, S. Kajiyama, H. Iinuma, E. Hosono, S. Oro, I. Moriguchi, M. Okubo and A. Yamada, *Nat. Commun.*, 2015, **6**, 1–3.
- 45 F. Shahzad, M. Alhabeab, C. B. Hatter, B. Anasori, S. M. Hong, C. M. Koo and Y. Gogotsi, *Science*, 2016, **353**, 1137–1140.
- 46 Y. Qing, W. Zhou, F. Luo and D. Zhu, *Ceram. Int.*, 2016, **42**, 16412–16416.
- 47 X. Sun, Y. Liu, J. Y. Zhang, L. R. Hou, J. F. Sun and C. Z. Yuan, *Electrochim. Acta*, 2019, **295**, 237–245.
- 48 X. Sun, K. Tan, Y. Liu, J. Y. Zhang, D. K. Denis, F. U. Zaman, L. R. Hou and C. Z. Yuan, *Nanoscale*, 2019, **11**, 16755–16766.
- 49 B. Xiao, Y. C. Li, X. F. Yu and J. B. Cheng, *Chem. Sci.*, 2016, **235**, 103–109.
- 50 J. Chen, K. Chen, D. Tong, Y. Huang, J. Zhang, J. Xue, Q. Huang and T. Chen, *Chem. Sci.*, 2015, **51**, 314–317.
- 51 S. Devaraj and N. Munichandraiah, *J. Phys. Chem. C*, 2008, **112**, 4406–4417.
- 52 T. Brousse, M. Toupin and R. Dugas, *J. Electroanal. Chem.*, 2006, **153**, A2171–A2180.
- 53 S. L. Kuo and N. L. Wu, *J. Electroanal. Chem.*, 2006, **153**, A1317–A1324.
- 54 M. Khazaei, M. Araim and T. Sasaki, *Adv. Funct. Mater.*, 2012, **23**, 2815–2819.
- 55 Y. Xie, M. Naguib and V. N. Mochalin, *J. Am. Chem. Soc.*, 2014, **136**, 6385–6394.
- 56 C. J. Xu, H. D. Du and B. H. Li, *J. Electrochem. Soc.*, 2009, **156**, A73–A78.
- 57 O. Ghodbane, J. L. Pascal and F. Favier, *ACS Appl. Mater. Interfaces*, 2009, **1**, 1130–1139.
- 58 C. E. Ren, K. B. Hatzell, M. Alhabeab, Z. Ling, K. A. Mahmoud and Y. Gogotsi, *J. Phys. Chem. Lett.*, 2015, **6**, 4026–4029.
- 59 J. Luo, W. Zhang, H. Yuan, C. Jin, L. Zhang, H. Huang, C. Liang, Y. Xia, J. Zhang, Y. Gan and X. Tao, *ACS Nano*, 2017, **11**, 2459–2463.

